Materials Advances

ROYAL SOCIETY OF CHEMISTRY

PAPER

View Article Online
View Journal | View Issue

Cite this: *Mater. Adv.*, 2024, 5, 6222

High-performance anthracene-linked covalent triazine frameworks with dual functions for CO_2 capture and supercapacitor applications†

Ming-Chieh Lin, [a] Shiao-Wei Kuo *[ab] and Mohamed Gamal Mohamed *[ac]

Received 2nd June 2024,
Accepted 21st June 2024

DOI: 10.1039/d4ma00565a

rsc.li/materials-advances

Porous nitrogen-rich materials with high conductivity have enormous potential as electrode materials for supercapacitors. However, the effectiveness of these materials depends on their N content and surface area. To overcome these challenges, by employing an ionothermal reaction at 500 °C and utilizing different molar ratios of $ZnCl_2$, we successfully synthesized porous covalent triazine frameworks (ANT-CTFs) using 2,3,6,7,9,10-hexacyanoanthracene (ANT-6CN) units. This synthetic approach led to the formation of two distinct microporous materials known as ANT-CTF-10-500 and ANT-CTF-20-500. The thermogravimetric analysis (TGA) and BET tests confirmed that the ANT-CTFs possessed substantial surface areas, falling within the range of 106 to 170 m^2 g^{-1}. Additionally, these materials exhibited remarkable thermal stability, resulting in char yields of up to 81 wt%. Additionally, ANT-CTF-10-500 exhibited an impressive capacitance of 81.2 F g^{-1}, along with excellent cycle stability (up to 87% capacitance retention). Furthermore, the material showed CO_2 adsorption capabilities, with an uptake of up to 2.14 mmol g^{-1}. The ANT-CTFs offer a competitive option for applications involving CO_2 uptake and electrochemical energy storage.

Introduction

In recent years, environmental awareness has risen, and renewable energy is seen as a key to sustainable development. One of the problems faced by the development of renewable energy is the capacity improvement of energy storage systems. Supercapacitors belong to one of the electromagnetic energy storage systems.[1] The energy storage of supercapacitors uses a special electrode structure such as porous materials, which possess a high specific surface area, thereby generating a large capacitance. The technical characteristics are fast charging and discharging speed, high cycle usage, and that when used in transportation, they can quickly discharge during acceleration and recover energy during braking. Even frequent acceleration and braking will not affect the battery life, but the high cost is still the key factor that prevents it from being widely used. Scientists worldwide are searching for stable and high-capacitance materials for energy storage devices. Electric double-layer capacitors (EDLCs), a specific type of supercapacitor, are an emerging technology that offers a wide range of operating temperatures, high energy densities, substantial power densities, and stable cycling performance.[2–5] EDLCs utilize mobile electrolyte ions to store charged particles at the interface between the electrolyte and electrode.[2–7] Researchers have evaluated numerous studies to develop energy storage systems that are both highly sustainable and efficient. These studies have focused on a range of materials, including metal oxides and their hybrid materials,[8–13] metal–organic frameworks (MOFs),[14–18] porous organic polymers (POPs),[19–23] and other carbon-based materials.[24–32] The majority of porous carbon materials have distinct specific capacitance, but when the surface area and porosity increase owing to the breakdown of conductive pathways the electrical conductivity declines. This limits their power capability. To improve the energy density and power output, investigations have been carried out by researchers to explore the incorporation of functional groups or heteroatoms into porous materials to induce pseudocapacitance.[33–38] When incorporated, these heteroatoms can alter the properties of porous materials by acting as electron donors and acceptors, leading to the manifestation of pseudocapacitive behavior.[39,40] Environmental issues are increasingly drawing scholarly attention, especially with the

[a] *Department of Materials and Optoelectronic Science, College of Semiconductor and Advanced Technology Research, Center for Functional Polymers and Supramolecular Materials, National Sun Yat-Sen University, Kaohsiung 804, Taiwan. E-mail: kuosw@faculty.nsysu.edu.tw, mgamal.eldin12@yahoo.com, mgamal.eldin12@aun.edu.eg*

[b] *Department of Medicinal and Applied Chemistry, Kaohsiung Medical University, Kaohsiung 807, Taiwan*

[c] *Chemistry Department, Faculty of Science, Assiut University, Assiut 71516, Egypt*

† Electronic supplementary information (ESI) available. See DOI: https://doi.org/10.1039/d4ma00565a

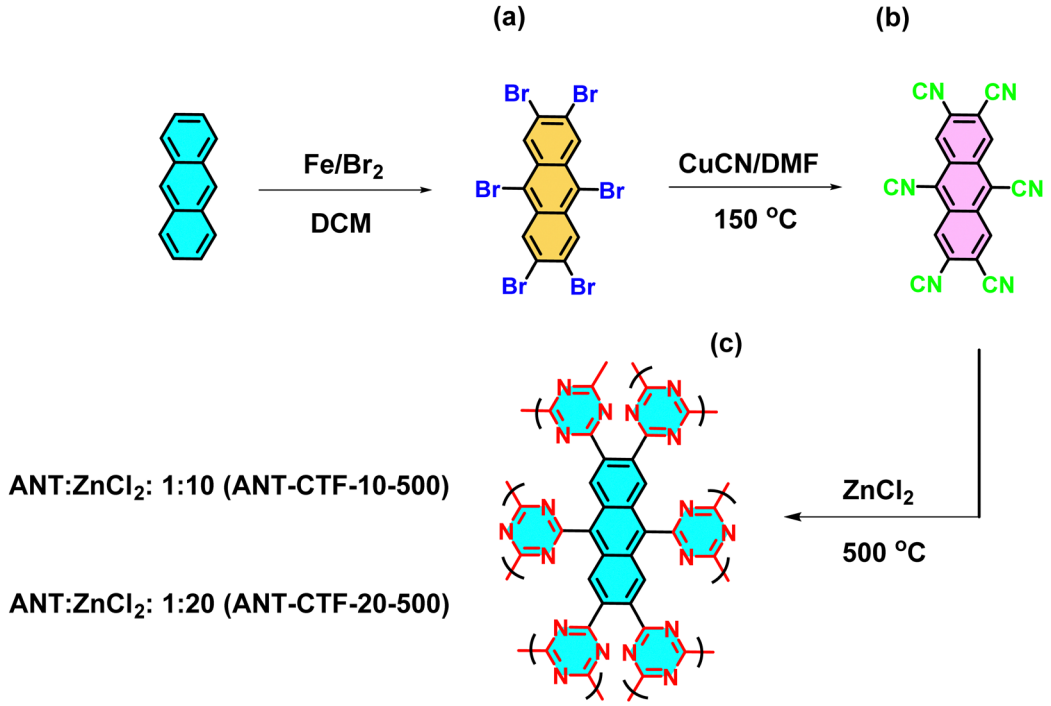

Fig. 1 Preparation method and reaction conditions of ANT-Br_6 (a), ANT-6CN (b), and ANT-CTFs (c) from ANT monomer.

rise of global warming and the ongoing industrial revolution being highlighted as significant problems. The main drivers of global warming are greenhouse gases such as CO_2, N_2O, and CH_4.[41–44] Among these, CO_2 is undeniably the principal contributor to both climate change and global warming, with its atmospheric concentration rising rapidly.[41–44] Therefore, novel POPs and CTFs are gaining attention for their potential use in energy storage, gas capture, and other applications. This kind of material possesses distinctive characteristics, including high surface area, extensive porosity, high mechanical stability, and low density.[45–51]

Under ionothermal conditions, CN groups undergo cyclotrimerization, giving rise to CTFs that find applications across various disciplines, such as gas storage application, sensing, heterogeneous catalysis, and electrocatalysis for oxygen reduction reactions, CO_2 absorption and conversion, lithium batteries, and supercapacitors.[52–57] Li *et al.* documented the synthesis of COF materials demonstrating remarkable characteristics, including high surface area, well-defined pore structures, and exceptional cycling stability, even after undergoing 7000 cycles.[58] Bhanja *et al.* synthesized COFs using triazine units that displayed high porosity and conjugation, resulting in a capacitance of 354 F g^{-1}. The material also demonstrated exceptional cycling stability, maintaining 95% capacity retention after numerous cycles.[59] Apart from the above research, Vargheese *et al.* synthesized a category of triazine-based COFs, exhibiting noteworthy attributes such as high specific capacitance, excellent cycling stability, and a substantial surface area of 711 m^2 g^{-1}.[60] The rigid, π-conjugated surface of the anthracene (ANT) molecule contributes to its high charge transfer efficiency and significant fluorescence emission.[61] Mohamed *et al.* discovered that An-CTF-10-500 exhibits a capacitance of 589 F g^{-1} and a high CO_2 adsorption capacity.[62] Hence, we developed a new type of material called nitrogen-enriched CTF using the ANT moiety and molten $ZnCl_2$ at a high temperature of 500 °C with two different molar ratios (1 : 10 and 1 : 20), as presented in Fig. 1. We selected molten $ZnCl_2$ as the reaction medium for the trimerization of ANT-6CN due to its high solubility and moderate Lewis acidity.[63] Subsequently, a comprehensive investigation was conducted on the various attributes of the ANT-CTFs. This encompassed the examination of their chemical structure, composition, thermal stability, crystallinity, surface area, and porosity. To achieve this, a diverse array of analytical techniques such as FTIR, TGA, XRD, Raman spectroscopy, XPS, SEM, TEM, and BET theory were employed. Furthermore, we also tested their electrochemical performance for energy storage and CO_2 uptake for gas storage applications.

Experimental section

Materials

Copper(I) cyanide (CuCN), ethylenediamine, iron (Fe) powder, anthracene (ANT), bromine solution (Br_2), dichloromethane (DCM), sodium thiosulfate ($Na_2S_2O_3$), *N*,*N*-dimethylformamide (DMF), zinc chloride ($ZnCl_2$), HCl solution (37%), methanol, and ethanol were purchased from different companies (Sigma-Aldrich, USA and Alfa Aesar, UK).

Preparation of 2,3,6,7,9,10-hexabromoanthracene (ANT-Br_6)[64]

In 190 mL of dry DCM, a flask containing ANT (2 g), iron powder (4.23 g), and Br_2 (4.11 mL) was agitated under nitrogen

for 6 h at room temperature. The mixture was quenched with $Na_2S_2O_3$ (10%). After the reaction, the obtained gray solid was washed with water to produce ANT-Br_6 (71%) as a gray powder. The gray product was not further purified due to its poor insolubility.

Preparation of 2,3,6,7,9,10-hexacyanoanthracene (ANT-6CN)

CuCN (8.9 g) and ANT-Br_6 (5 g) were blended and refluxed at 150 °C for two days in the presence of 150 mL of DMF in a flask. The resulting DMF solution was combined with ethylenediamine and water, leading to the formation of a brown solid after cooling and the subsequent removal of excess CuCN by filtration. The brown solid was further boiled and crystallized in DMF solution, resulting in the formation of brown needle-like ANT-6CN.

Preparation of ANT-CTFs

To prepare ANT-CTFs, we mixed ANT-6CN with anhydrous $ZnCl_2$, and regulating the molar ratios of 0.1 and 0.05, respectively. The mixture was subjected to a specific temperature of 500 °C and maintained under the same conditions in a nitrogen atmosphere for 2 days to obtain ANT-CTFs (Fig. 1). The obtained black solid was immersed in HCl (1 M), water, and acetone for 48 h, yielding ANT-CTFs in the form of a black powder.

Results and discussion

Preparation and characterization of ANT-6CN and ANT-CTFs

Based on previous research, the CTF materials exhibited remarkable characteristics, such as thermal stability, outstanding cycling stability, and porosity properties.[62] Therefore, we were keen to extend the research by increasing the triazine content and strengthening the crosslinking framework to investigate whether these properties improved. Fig. 1 shows the preparation procedure of the ANT-CTFs used in this research. The ANT compound [Fig. 1(a)] was converted into ANT-Br_6 through a bromine reaction in DCM and Fe powder [Fig. 1(b)]. Then, the ANT-Br_6 compound was converted into ANT-6CN in the presence of dry DMF and CuCN [Fig. 1(c)].

After that, the ionothermal synthesis was conducted for trimerization of the CN groups of ANT-6CN in different ratios of $ZnCl_2$ at 500 °C, acquiring ANT-CTF materials [Fig. 1(c)]. The FTIR spectra of ANT-6CN and the obtained ANT-CTFs are shown in Fig. 2(a). The band positioned at 2223 cm^{-1} on the FTIR profile corresponds to the nitrile group in the ANT-6CN

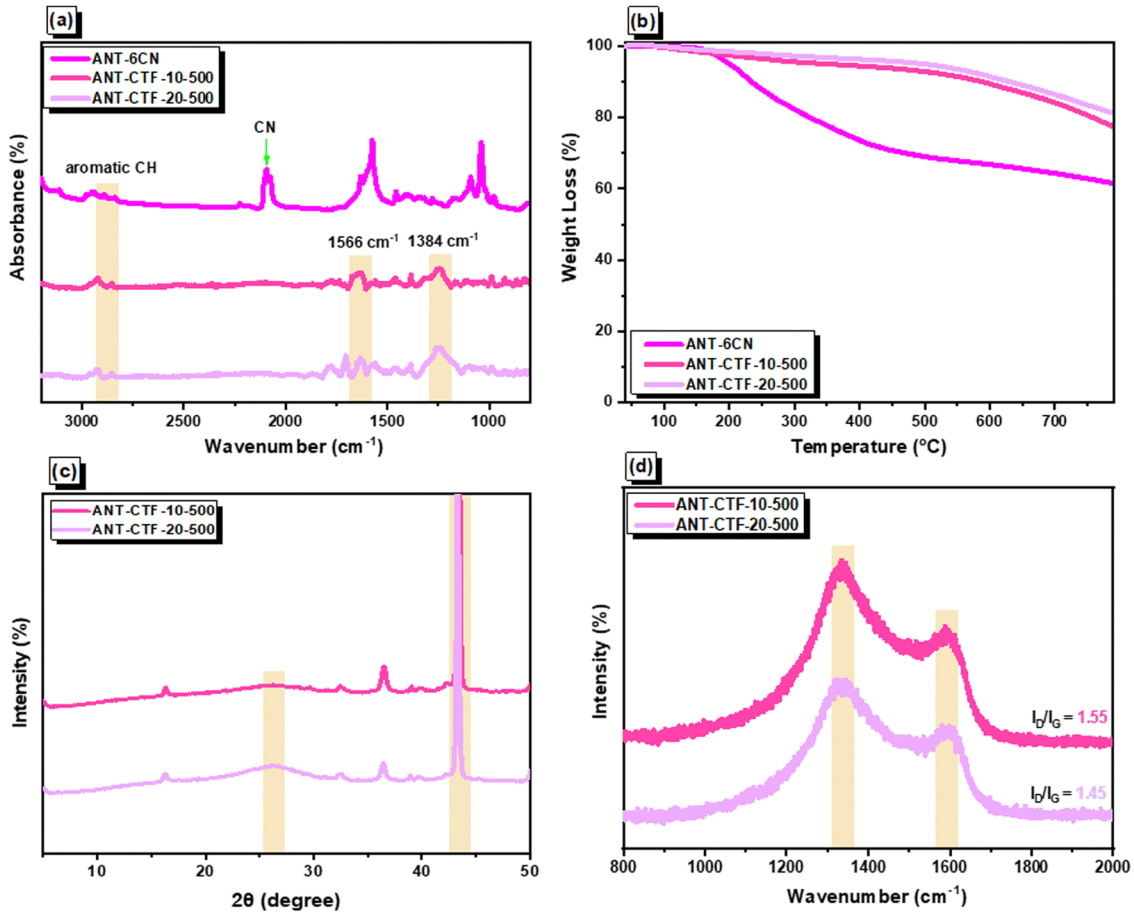

Fig. 2 (a) FTIR and (b) TGA profiles ANT-6CN, ANT-CTF-10-500, and ANT-CTF-20-500. (c) XRD and (d) Raman profiles of ANT-CTF-10-500, and ANT-CTF-20-500.

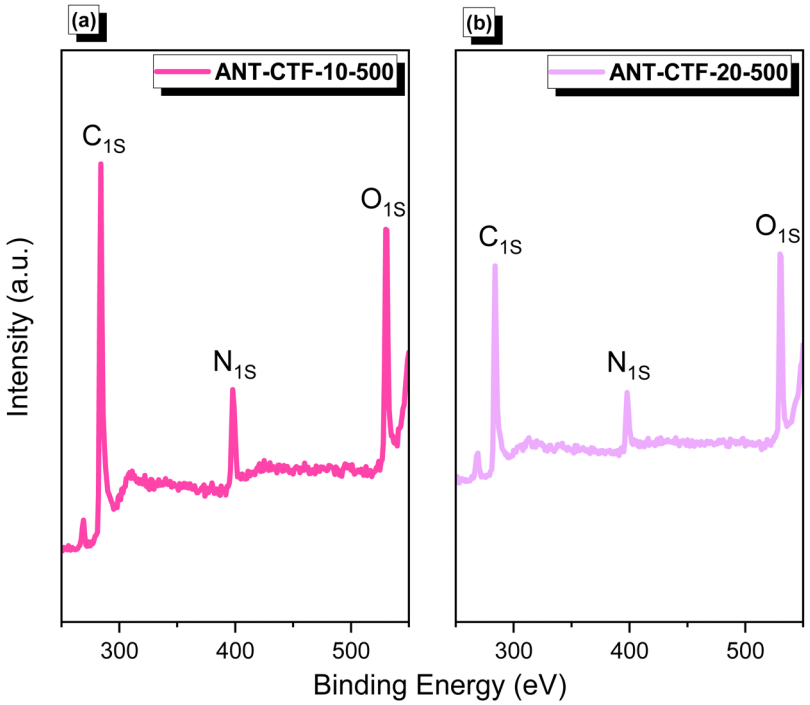

Fig. 3 XPS profiles of ANT-CTF-10-500 (a) and ANT-CTF-20-500 (b).

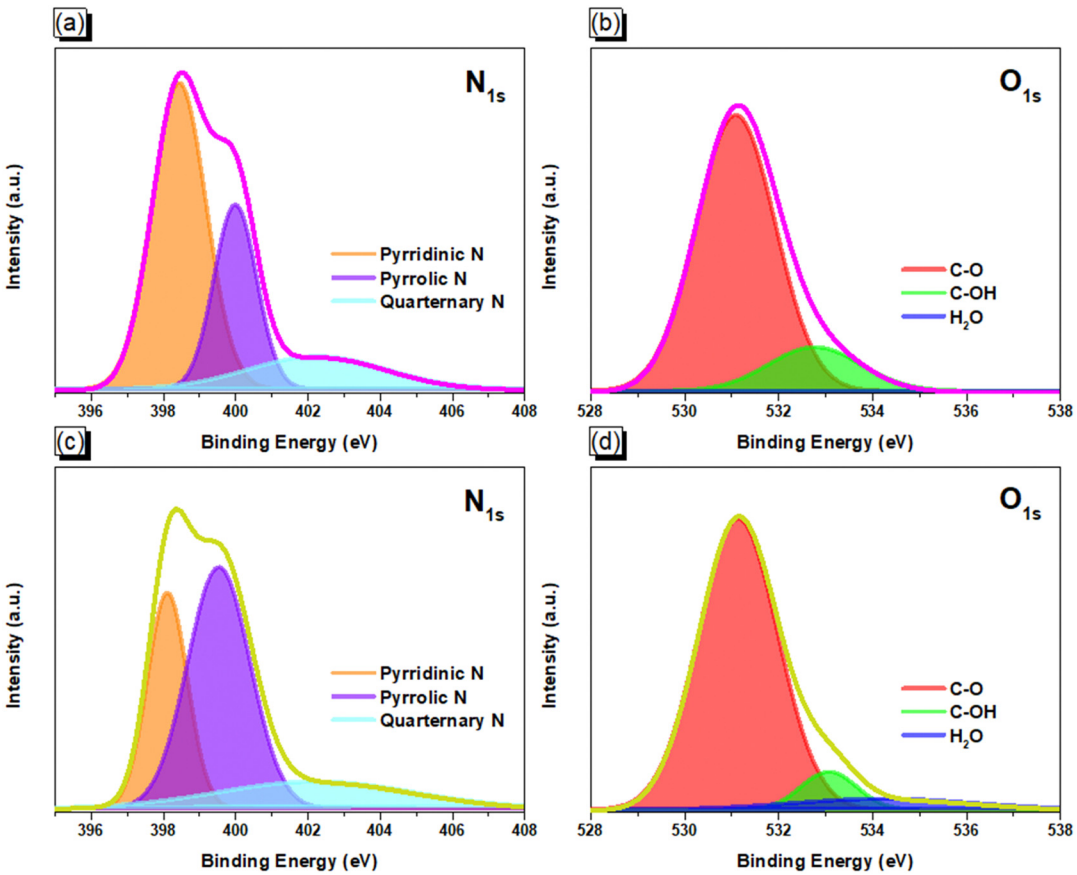

Fig. 4 XPS fitting curves of N 1s and O 1s orbitals for ANT-CTF-10-500 (a) and (b) and ANT-CTF-20-500 (c) and (d).

structure, which also confirmed its successful synthesis. In addition, aromatic stretching signals were also found at 1600 and 1455 cm^{-1}. On the other hand, the presence of bands at 1566 and 1384 cm^{-1} in the FTIR spectra played a crucial role in identifying the presence of triazine units in each ANT-CTF, which also confirms that the nitrile group underwent cyclization.[65,66] For further study on thermal stability, the synthesized ANT-6CN and ANT-CTFs were introduced to perform TGA analysis from 40 to 800 °C under N_2. As shown in Fig. 2(b), the ANT-6CN monomer had a T_{d10} of 234 °C and a 62 wt% char yield. After calcination, the T_{d10} of ANT-CTF-10-500 and ANT-CTF-20-500 improved to reach 588 °C and 630 °C, and their char yields increased to 77 and 81 wt%; respectively. All TGA data of ANT-6CN and ANT-CTFs are collected in Table S1 (ESI†). Fig. 2(c) shows the XRD patterns of the ANT-CTFs, where the (002) and (100) planes of hexagonal graphitic carbon are represented by the two distinctive diffraction peaks at around $2\theta = 26^\circ$ and 43°, respectively.[67] To evaluate the graphitization degree and defective properties of carbon materials, Raman spectroscopy is often considered a crucial approach. Fig. 2(d) shows the Raman spectra of the ANT-CTFs, recorded from 800 to 2000 cm^{-1}. Both ANT-CTFs exhibit two prominent peaks at around 1335 cm^{-1} (D band) and 1590 cm^{-1} (G band), which indicate the presence of a graphitic structure.[68–70] For ANT-CTF-10-500 and ANT-CTF-20-500, the I_D/I_G ratios were found to be 1.55 and 1.48, respectively. This suggests that ANT-CTF-10-500 has a higher degree of graphitization, indicating a lower level of defects in its morphology and a greater condensed aromatic structure than ANT-CTF-20-500 and other reported CTFs.[65,66,71–74] The XPS spectra of the synthesized ANT-CTFs are shown in Fig. 3. There were three peaks corresponding to the carbon atom, the C–N bond for the N 1s orbital belonging to the triazine unit and the O 1s orbital belonging to moisture and oxygen, which were located at 284 eV, 400 eV, and 530 eV, respectively.[65,66,71–74] Fig. 4(a–d) and Table S2 (ESI†) provide the XPS curve fitting for N 1s and O 1s orbitals, enabling the assessment of the chemical composition of the ANT-CTFs. Based on the investigation, three different N species were found: hexagonal pyridinic N species, quaternary N species (at 401.5 eV), and pyrrolic species (at 400 eV). After analyzing the data, it was found that pyridinic N was the most abundant type of nitrogen in ANT-CTF-10-500 [Fig. 4(a)], while

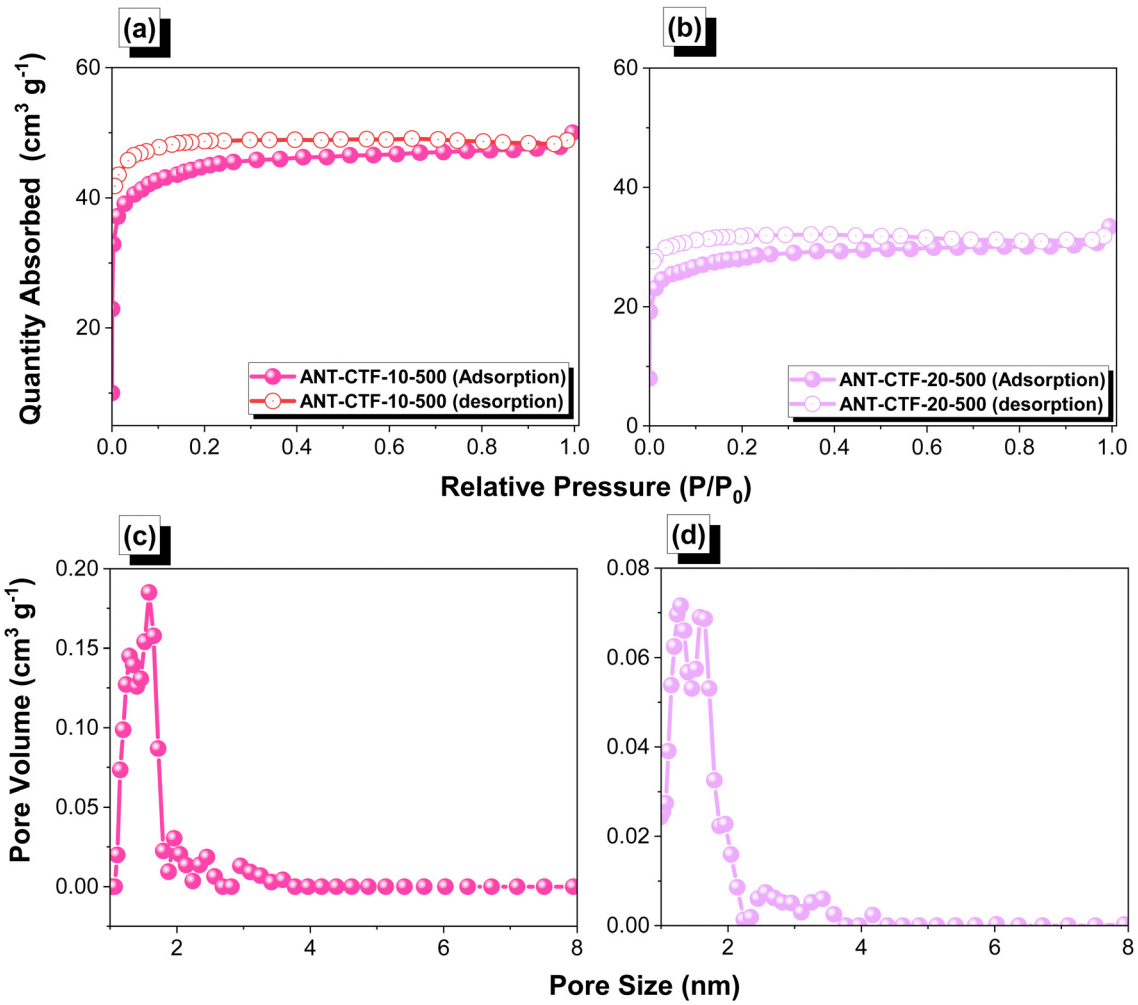

Fig. 5 (a, b) N_2 adsorption–desorption isotherms and (c, d) pore size analyses of ANT-CTF-10-500 (a, c) and ANT-CTF-20-500 (b, d).

pyrrolic N dominated in ANT-CTF-20-500 [Fig. 4(c)]. Furthermore, the surface of these ANT-CTFs revealed the presence of three different oxygen species, as indicated by the distinct peaks observed in Fig. 4(b) and (d). These peaks were associated with absorbed oxygen (531.5 eV), moisture (533 eV), and a C–O single bond (535 eV), respectively.[65,75]

Porosity and CO_2 capture ability of ANT-CTF-10-500 and ANT-CTF-20-500

After confirming the synthesis of ANT-CTFs, we proceeded with our study to measure the porosity of the ANT-CTF materials [Fig. 5(a–d)]. As shown in Fig. 5(a) and (b), both ANT-CTFs had type I isotherms according to the IUPAC classification of BET isotherms. The results shown in Table 1 illustrate the surface areas for both ANT-CTF precursors. ANT-CTF-10-500 and ANT-CTF-20-500 had BET surface areas (SA_{BET}) of 170 and 106 $m^2\ g^{-1}$, respectively. The anticipated factors contributing to the diminished surface area and crystallinity in ANT-CTF materials are the triazine groups, which can, in part, result from significant steric hindrance effects during synthesis, potentially leading to structural disorder. The higher SA_{BET} of ANT-CTF-10–500 as compared to ANT-CTF-20-500 can be attributed to the denser nanoparticle packing and the higher number of defects in the ANT-CTF-10-500 framework.[62,65,75] Furthermore, the pore sizes of both ANT-CTFs based on NLDFT theory were all 1.28–1.6 nm [Fig. 5(c) and (d)], which were classified as micropores and observed reasonably on the BET curves increasing sharply at lower relative pressure. The SEM images of the obtained ANT-CTFs are presented in Fig. 6(a–d). Focusing on ANT-CTF-10-500, although it seems to have an irregular block shape and there are no obvious cavities on the surface of the material [Fig. 6(a)], the porous structure was found on the section of the bulk shown in Fig. 6(b). As shown in Fig. 6(c) and (d), ANT-CTF-20-500 exhibits an irregular, rough surface with obvious cavities. Furthermore, HR-TEM revealed the presence of random micropores of these ANT-CTF samples shown in Fig. 7(a–f), which corresponds to the pore size analysis. The presence of C, N, and O atoms and their distribution in the ANT-CTF frameworks were identified by the SEM–EDS mapping data displayed in Fig. S1 and S2 (ESI†). We examined the stability of ANT-CTFs in a 1 M KOH solution, employing XRD, SEM, and BET analyses, with the results presented in Fig. S3–S6 (ESI†). From Fig. S3 (ESI†), it is evident that two distinctive diffraction peaks at around $2\theta = 26^\circ$ and 43° have persisted. Notably, both ANT-CTF variants, specifically ANT-CTF-10-500 and ANT-CTF-20-500,

Table 1 Surface area, pore size, and CO_2 uptake of ANT-CTFs

Sample	Surface area ($m^2\ g^{-1}$)	Pore size (nm)	CO_2 uptake (298 K) (mmol g^{-1})	CO_2 uptake (273 K) (mmol g^{-1})
ANT-CTF-10-500	170	1.28, 1.55	1.45	2.14
ANT-CTF-20-500	106	1.26, 1.6	0.88	1.29

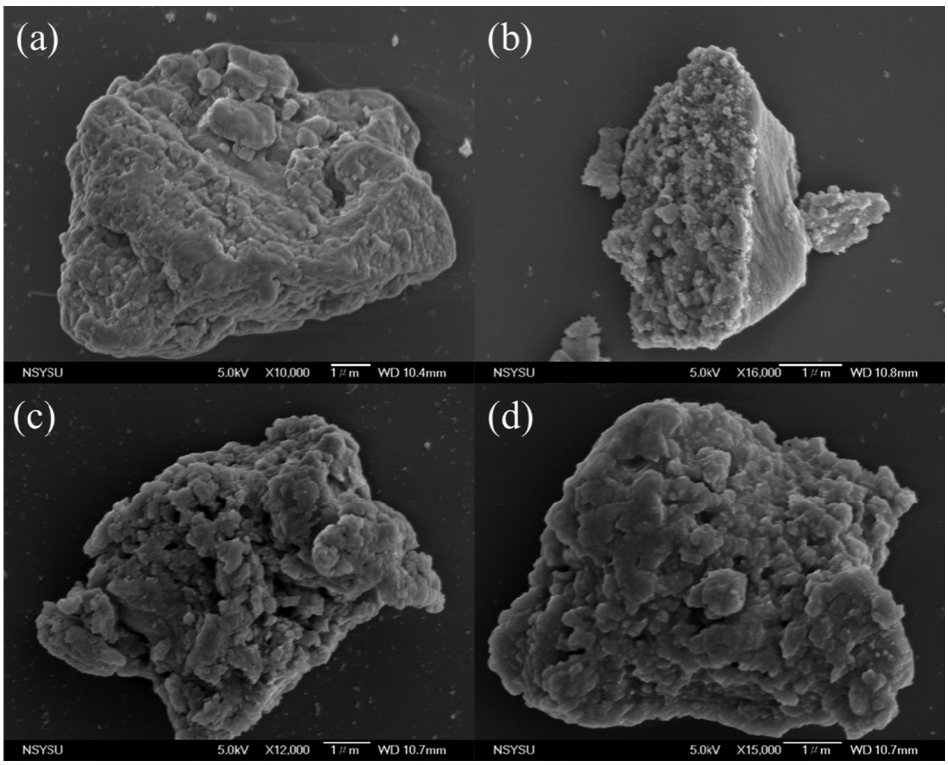

Fig. 6 SEM images of ANT-CTF-10-500 (a) and (b) and ANT-CTF-20-500 (c) and (d).

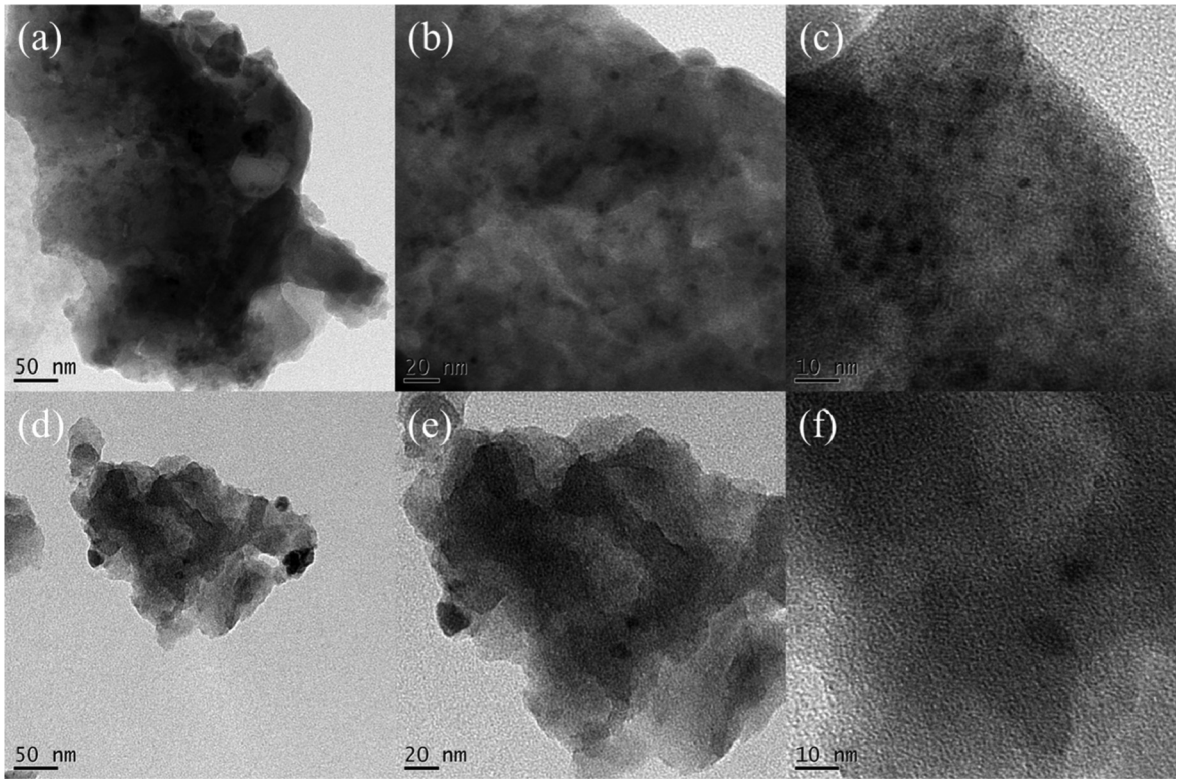

Fig. 7 TEM images at different scales of ANT-CTF-10-500 (a)–(c) and ANT-CTF-20-500 (d)–(f).

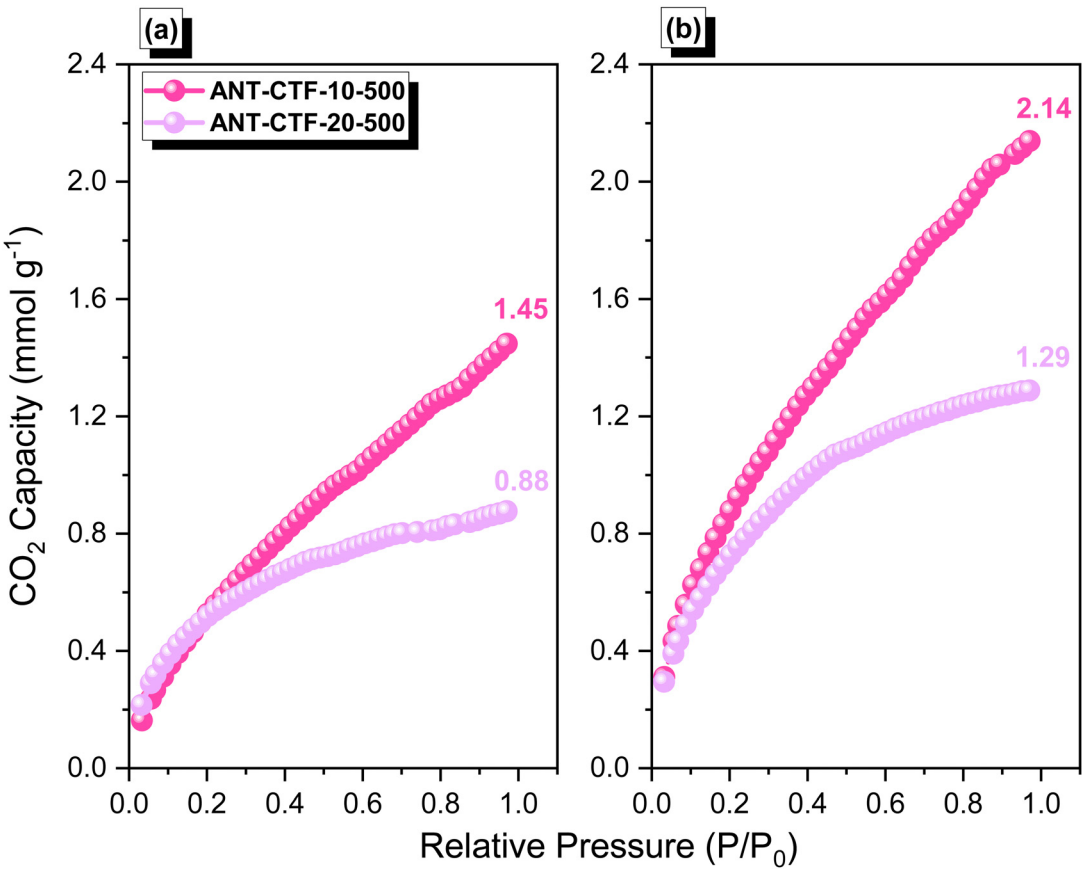

Fig. 8 CO_2 adsorption performance of ANT-CTF-10-500 and ANT-CTF-20-500 at 298 K (a) and 273 K (b).

featured a framework containing O, N, and C atoms, as exemplified in Fig. S4 and S5 (ESI†). ANT-CTF-10-500 exhibited a S_{BET} of 160 $m^2\ g^{-1}$, while ANT-CTF-20-500 displayed a slightly lower S_{BET} of 95 $m^2\ g^{-1}$ [Fig. S6, ESI†]. We obtained CO_2 uptake profiles for all of these ANT-CTFs at 298 K and 273 K to determine their potential for CO_2 uptake. ANT-CTF-10-500 and ANT-CTF-20-500 demonstrated CO_2 capture performances of 1.45 and 0.88 mmol g^{-1} at 298 K, respectively, as shown in Fig. 8(a), Table 1, and Table S3 (ESI†). At 273 K, the CO_2 capture capacities of ANT-CTF-10-500 and ANT-CTF-20-500 were 2.14 and 1.29 mmol g^{-1}, respectively, shown in Fig. 8(b). The greater S_{BET} of 170 $m^2\ g^{-1}$ for ANT-CTF-10-500 enhanced the interaction between CO_2 and the material framework, thereby increasing the CO_2 absorption compared to ANT-CTF-20-500.[65,66,75]

Table S3 (ESI†) provides a summary of the performance of ANT-CTFs in terms of their CO_2 uptake capabilities, offering a comparative assessment against other porous precursors. Table S3 (ESI†) shows that our ANT-CTF-10-500 exhibited a higher CO_2 adsorption capacity compared to FEC-Mel POP, FEC-PBDT POP, RIO-13, RIO-12, RIO-11 m, and RIO-11, but it was lower than those of CTF-5-400 and CTF-10-400.[62,75–77] According to the Clausius–Clapeyron equation, the isosteric heat of adsorption (Q_{st}) for ANT-CTF-10-500 and ANT-CTF-20-500 was determined to be 27 kJ mol^{-1} and 19 kJ mol^{-1}, respectively, at a low CO_2 adsorption level of approximately 0.4 mmol g^{-1} based on their CO_2 adsorption results at 298 K and 273 K. The data highlight a significant level of interaction between the CO_2 molecules and our ANT-CTF frameworks, as detailed in Table S4 (ESI†). The results show that the numerical value for ANT-CTF-10-500 exceeds that of ANT-CTF-20-500, which correlates with the superior CO_2 adsorption performance observed for ANT-CTF-10-500. Additionally, the isosteric heat of adsorption value for ANT-CTF-10-500 not only surpasses the liquefaction heat of bulk CO_2 (17 kJ mol^{-1}) but also exceeds those of several other CTF materials. This indicates relatively strong interactions between CO_2 and our ANT-CTFs, more so than some other reported porous organic frameworks. After six measurement cycles at 25 °C [Fig. S7, ESI†], the CO_2 adsorption capacity of ANT-CTF-10-500 decreased from 1.45 to 0.88 mmol g^{-1}, while ANT-CTF-20-500 exhibited a reduction from 0.88 to 0.69 mmol g^{-1}.

Electrochemical performance of the ANT-CTF-10-500 and ANT-CTF-20-500

The electrochemical performance of the ANT-CTF samples as supercapacitor electrode materials was carefully investigated through cyclic voltammetry (CV) and galvanostatic charge–discharge (GCD). The tests were conducted in a 1 M KOH

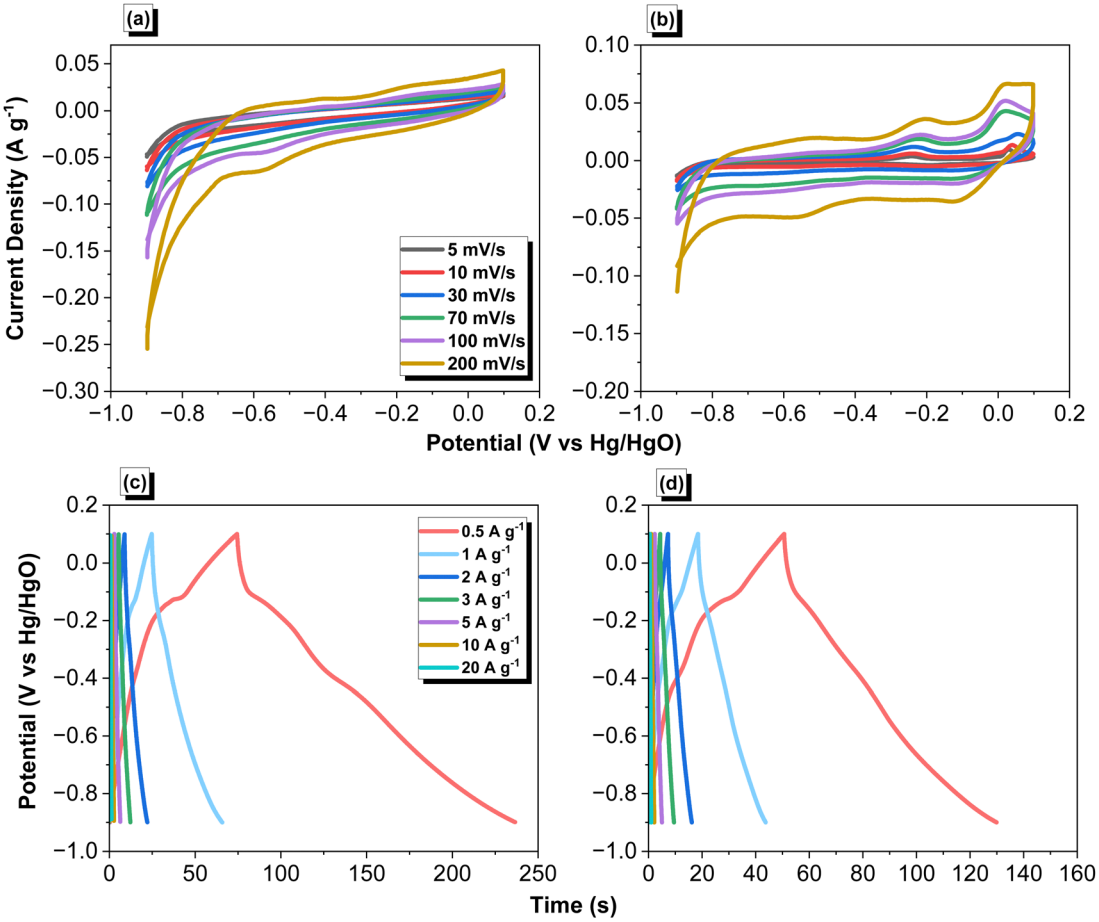

Fig. 9 Electrochemical performance of ANT-CTF-10-500 (a) and (c) and ANT-CTF-20-500 (b) and (d) through (a) and (b) CV and (c) and (d) GCD.

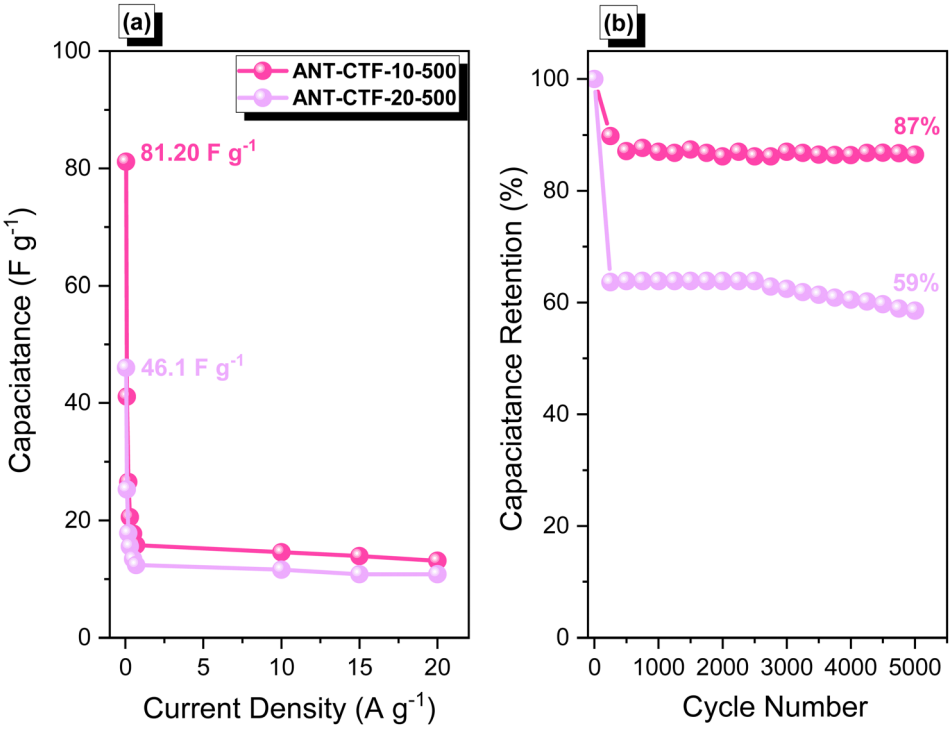

Fig. 10 Specific capacitance (a) and capacitance retention (b) of ANT-CTF-10-500 and ANT-CTF-20-500.

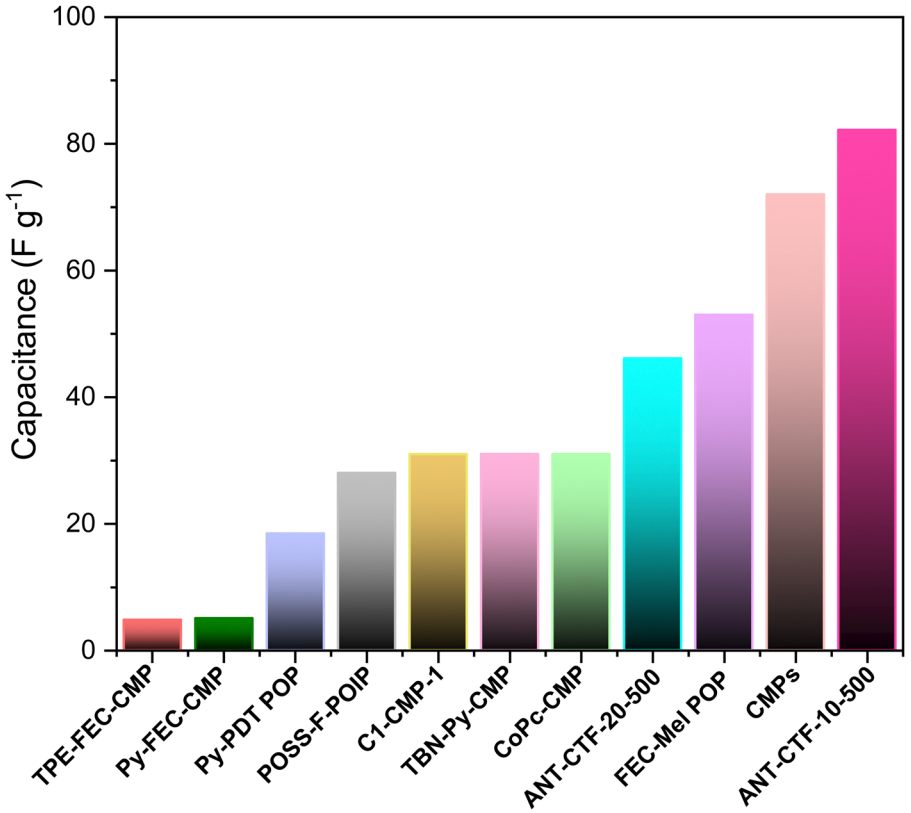

Fig. 11 ANT-CTF materials showing significantly superior capacitance values compared to other porous organic electrode precursors.

aqueous electrolyte within the potential range of −1 to 0.2 V. The corresponding CV patterns of the ANT-CTF samples are presented in Fig. 9(a) and (b), recorded at various sweep rates ranging from 5 to 200 V s^{-1}. The rectangle-like shape with an anodic peak in the CV curves of both ANT-CTF samples suggested that their capacitive response was mainly due to electric double-layer capacitance (EDLC), with minimal pseudocapacitance resulting from different nitrogen and oxygen species.[58,59] The reaction of ANT-6CN with $ZnCl_2$ produces a unique carbon framework with pyridinic nitrogen atoms akin to those found in N-doped carbon materials.[65,66] XPS, SEM–EDS mapping, and BET investigations all revealed that the ANT-CTF samples had N-heteroatom frameworks and high specific surface areas. As shown in Fig. 9(c) and (d), the GCD curves of ANT-CTF samples were examined at various current densities ranging from 0.5 to 20 A g^{-1}. The curves exhibited a triangular form and a few small bends, which showed that both EDLC and pseudocapacitance properties were present.[64–86] The capacitances of ANT-CTF samples which were calculated and determined from the GCD curves are shown in Fig. 10(a). At 0.5 A g^{-1}, ANT-CTF-10-500 displayed a superior capacitance value of 81.20 F g^{-1}. The enhanced performance observed can be attributed to multiple factors such as increased SA_{BET}, higher pore size, and the presence of various functional groups, including phenolic OH groups, and pyridinic and pyrrolic nitrogen atoms, within the graphitic microporous carbon structures of ANT-CTF-10-500. These structural characteristics improve the interactions between the electrolyte and the electrode material, which in turn can enhance the overall performance and ionic conductivity of the storage system. In contrast, ANT-CTF-20-500 exhibited almost half the specific capacitance of the former. As the current density increased from 0.5 to 20 A g^{-1}, Fig. 10(a) demonstrates that the specific capacitances of ANT-CTF samples tended to gradually decrease. This was likely caused by the electrolyte ions adhering quickly to the electrodes. On the other hand, ANT-CTF-10-500 performed better due to its larger surface area during the cycling test. The long-term stability of the ANT-CTF electrode materials was also evaluated by analyzing the GCD profiles of both ANT-CTF materials at 10 A g^{-1} (over 5000 cycles). Fig. 10(b) displays the extraordinary stability of ANT-CTF-10-500 in the KOH electrolyte, which still retained 86.5% of its original capacity after the cycling test.

From Fig. 11, it is evident that ANT-CTF materials outperform other porous organic electrode precursors, showing significantly higher capacitance values.

Conclusions

We have successfully developed porous covalent triazine frameworks (ANT-CTFs) as potential electrode materials for gas capture and supercapacitors. By utilizing ANT-6CN under an ionothermal reaction in the presence of $ZnCl_2$ at 500 °C, we obtained two distinct microporous materials: ANT-CTF-10-500 and ANT-CTF-20-500. TGA and BET analyses revealed exceptional thermal stability with char yields of up to 81 wt% and high specific surface areas ranging from 106 to 170 m^2 g^{-1} for these ANT-CTFs. ANT-CTF-10-500 displayed a notable CO_2 adsorption capacity of up to 2.14 mmol g^{-1} (273 K) and showed impressive electrochemical properties, including a specific capacitance of 81.20 F g^{-1} and a remarkable cycle stability of 87% after 5000 cycles. These results demonstrate the considerable potential of ANT-CTF-10-500 for both CO_2 uptake and electrochemical energy storage applications.

Author contributions

Ming-Chieh Lin: investigation, methodology. Shiao-Wei Kuo: supervision. Mohamed Gamal Mohamed: investigation, methodology, conceptualization, supervision, writing – original draft.

Data availability

Data are presented within the article or the ESI.†

Conflicts of interest

There are no conflicts to declare.

Acknowledgements

This study was supported financially by the National Science and Technology Council, Taiwan, under contracts NSTC 112-2223-E-110-002- and 112-2218-E-110-007. The authors thank the staff at National Sun Yat-sen University for their assistance with the TEM (ID: EM022600) experiments.

Notes and references

1 M. Ejaz, M. G. Mohamed, Y. T. Chen, K. Zhang and S. W. Kuo, *J. Energy Storage*, 2024, **78**, 110166.
2 M. G. Mohamed, T. H. Mansoure, Y. Takashi, M. M. Samy, T. Chen and S. W. Kuo, *Microporous Mesoporous Mater.*, 2021, **328**, 111505.
3 M. M. Samy, M. G. Mohamed, T. H. Mansoure, T. S. Meng, M. A. R. Khan, C. C. Liaw and S. W. Kuo, *J. Taiwan Inst. Chem. Eng.*, 2022, **132**, 104110.
4 M. Ejaz, M. G. Mohamed and S. W. Kuo, *Polym. Chem.*, 2023, **14**, 2494–2509.
5 M. G. Mohamed, W. C. Chang, S. V. Chaganti, S. U. Sharma, J. T. Lee and S. W. Kuo, *Polym. Chem.*, 2023, **14**, 4589–4601.
6 L. Yao, Q. Wu, P. Zhang, J. Zhang, D. Wang, Y. Li, X. Ren, H. Mi, L. Deng and Z. Zheng, *Adv. Mater.*, 2018, **30**, 1706054.
7 M. G. Mohamed, E. C. Atayde Jr, B. M. Matsagar, J. Na, Y. Yamauchi, K. C. W. Wu and S. W. Kuo, *J. Taiwan Inst. Chem. Eng.*, 2020, **112**, 180–192.
8 C. An, Y. Zhang, H. Guo and Y. Wang, *Nanoscale Adv.*, 2019, **1**, 4644–4658.
9 Y. Wang, J. Guo, T. Wang, J. Shao, D. Wang and Y. W. Yang, *Nanomaterials*, 2015, **5**, 1667–1689.

10 T. Cottineau, M. Toupin, T. Delahaye, T. Brousse and D. Bélanger, *Appl. Phys. A: Mater. Sci. Process.*, 2006, **82**, 599–606.
11 C. Lokhande, D. Dubal and O. S. Joo, *Curr. Appl. Phys.*, 2011, **11**, 255–270.
12 Y. Ma, X. Xie, W. Yang, Z. Yu, X. Sun, Y. Zhang, X. Yang, H. Kimura, C. Hou and Z. Guo, *Adv. Compos. Hybrid Mater.*, 2021, 1–19.
13 X. Lang, A. Hirata, T. Fujita and M. Chen, *Nat. Nanotechnol.*, 2011, **6**, 232–236.
14 L. Niu, T. Wu, M. Chen, L. Yang, J. Yang, Z. Wang, A. A. Kornyshev, H. Jiang, S. Bi and G. Feng, *Adv. Mater.*, 2022, **34**, 2200999.
15 K.-B. Wang, Q. Xun and Q. Zhang, *EnergyChem*, 2020, **2**, 100025.
16 L. Wang, Y. Han, X. Feng, J. Zhou, P. Qi and B. Wang, *Coord. Chem. Rev.*, 2016, **307**, 361–381.
17 T. TQiu, Z. Liang, W. Guo, T. Tabassum, S. Gao and R. Zou, *ACS Energy Lett.*, 2020, **5**, 520–532.
18 K. M. Choi, H. M. Jeong, J. H. Park, Y. B. Zhang, J. K. Kang and O. M. Yaghi, *ACS Nano*, 2014, **8**, 7451–7457.
19 A. I. Said, M. G. Mohamed, M. Madhu, P. N. Singh, S. V. Chaganti, M. H. Elsayed, W. L. Tseng, F. M. Raymo and S. W. Kuo, *Polymer*, 2024, **300**, 126988.
20 M. G. Mohamed, M. M. Samy, T. H. Mansoure, C. J. Li, W. C. Li, J. H. Chen, K. Zhang and S. W. Kuo, *Int. J. Mol. Sci.*, 2021, **23**, 347.
21 M. G. Mohamed, A. M. Elewa, M. S. Li and S. W. Kuo, *J. Taiwan Inst. Chem. Eng.*, 2023, **150**, 105045.
22 S. Y. Chang, A. M. Elewa, M. G. Mohamed, I. M. A. Mekhemer, M. M. Samy, K. Zhang, H. H. Chou and S. W. Kuo, *Mater. Today Chem.*, 2023, **33**, 101680.
23 M. M. Samy, I. M. A. Mekhemer, M. G. Mohamed, M. H. Elsayed, K. H. Lin, Y. K. Chen, T. L. Wu, H. H. Chou and S. W. Kuo, *Chem. Eng. J.*, 2022, **446**, 137158.
24 A. B. Fuertes and M. Sevilla, *ChemSusChem*, 2015, **8**, 1049–1057.
25 L. Liu, Z. Niu and J. Chen, *Chem. Soc. Rev.*, 2016, **45**, 4340–4363.
26 R. J. Mo, Y. Zhao, M. Wu, H. M. Xiao, S. Kuga, Y. Huang, J. P. Li and S. Y. Fu, *RSC Adv.*, 2016, **6**, 59333–59342.
27 J. Tang, T. Wang, R. R. Salunkhe, S. M. Alshehri, V. Malgras and Y. Yamauchi, *Chem. – Eur. J.*, 2015, **21**, 17293–17298.
28 Y. Zhu, S. Murali, M. D. Stoller, K. J. Ganesh, W. Cai, P. J. Ferreira, A. Pirkle, R. M. Wallace, K. A. Cychosz and M. Thommes, *Science*, 2011, **332**, 1537–1541.
29 M. M. Samy, M. G. Mohamed and S. W. Kuo, *Eur. Polym. J.*, 2020, **138**, 109954.
30 C. Gu, N. Huang, Y. Chen, H. Zhang, S. Zhang, F. Li, Y. Ma and D. Jiang, *Angew. Chem., Int. Ed.*, 2016, **55**, 3049–3053.
31 J. Tang, R. R. Salunkhe, J. Liu, N. L. Torad, M. Imura, S. Furukawa and Y. Yamauchi, *J. Am. Chem. Soc.*, 2015, **137**, 1572–1580.
32 R. R. Salunkhe, J. Lin, V. Malgras, S. X. Dou, J. H. Kim and Y. Yamauchi, *Nano Energy*, 2015, **11**, 211–218.
33 D. Hulicova-Jurcakova, M. Seredych, G. Q. Lu and T. J. Bandosz, *Adv. Funct. Mater.*, 2009, **19**, 438–447.
34 J. Han, L. L. Zhang, S. Lee, J. Oh, K. S. Lee, J. R. Potts, J. Ji, X. Zhao, R. S. Ruoff and S. Park, *ACS Nano*, 2013, **7**, 19–26.
35 Z. S. Wu, A. Winter, L. Chen, Y. Sun, A. Turchanin, X. Feng and K. Müllen, *Adv. Mater.*, 2012, **24**, 5130–5135.
36 L. F. Chen, X. D. Zhang, H. W. Liang, M. Kong, Q. F. Guan, P. Chen, Z. Y. Wu and S. H. Yu, *ACS Nano*, 2012, **6**, 7092–7102.
37 X. Zhao, Q. Zhang, C. M. Chen, B. Zhang, S. Reiche, A. Wang, T. Zhang, R. Schlögl and D. S. Su, *Nano Energy*, 2012, **1**, 624–630.
38 X. Zhao, Q. Zhang, B. Zhang, C. M. Chen, A. Wang, T. Zhang and D. S. Su, *J. Mater. Chem.*, 2012, **22**, 4963–4969.
39 L. Zhao, L. Z. Fan, M. Q. Zhou, H. Guan, S. Qiao, M. Antonietti and M. M. Antonietti, *Adv. Mater.*, 2010, **22**, 5202–5206.
40 S. L. Candelaria, B. B. Garcia, D. Liu and G. Cao, *J. Mater. Chem.*, 2012, **22**, 9884–9889.
41 A. O. Mousa, M. G. Mohamed, C. H. Chuang and S. W. Kuo, *Polymers*, 2023, **15**, 1891.
42 M. G. Mohamed, W. C. Chang and S. W. Kuo, *Macromolecules*, 2022, **55**, 7879–7892.
43 B. Ray, S. R. Churipard and S. C. Peter, *J. Mater. Chem. A*, 2021, **9**, 26498–26527.
44 R. D. Piacentini and A. S. Mujumdar, *Dry. Technol.*, 2009, **27**, 629–635.
45 J. F. Mike and J. L. Lutkenhaus, *J. Polym. Sci., Part B: Polym. Phys.*, 2013, **51**, 468–480.
46 A. Halder, M. Ghosh, A. Khayum M, S. Bera, M. Addicoat, H. S. Sasmal, S. Karak, S. Kurungot and R. Banerjee, *J. Am. Chem. Soc.*, 2018, **140**, 10941–10945.
47 M. H. Gharahcheshmeh and K. K. Gleason, *Adv. Mater. Interfaces*, 2019, **6**, 1801564.
48 S. W. Kuo, *Polym. Int.*, 2022, **71**, 393–410.
49 M. G. Mohamed, M. H. Elsayed, A. M. Elewa, A. F. M. EL-Mahdy, C. H. Yang, A. A. Mohammed, H. H. Chou and S. W. Kuo, *Catal. Sci. Technol.*, 2021, **11**, 2229–2241.
50 M. Ejaz, M. G. Mohamed, W. C. Huang and S. W. Kuo, *J. Mater. Chem. A*, 2023, **11**, 22868–22883.
51 M. G. Mohamed, M. M. Ahmed, W. T. Du and S. W. Kuo, *Molecules*, 2021, **26**, 738.
52 P. Katekomol, J. Roeser, M. Bojdys, J. Weber and A. Thomas, *Chem. Mater.*, 2013, **25**, 1542–1548.
53 A. Bhunia, V. Vasylyeva and C. Janiak, *Chem. Commun.*, 2013, **49**, 3961–3963.
54 L. Hao, S. Zhang, R. Liu, J. Ning, G. Zhang and L. Zhi, *Adv. Mater.*, 2015, **27**, 3190–3195.
55 S. N. Talapaneni, T. H. Hwang, S. H. Je, O. Buyukcakir, J. W. Choi and A. Coskun, *Angew. Chem., Int. Ed.*, 2016, **55**, 3106–3111.
56 C. Krishnaraj, H. S. Jena, K. Leus and P. Van Der Voort, *Green Chem.*, 2020, **22**, 1038–1071.
57 L. Guo, X. Wang, Z. Zhan, Y. Zhao, L. Chen, T. Liu, B. Tan and S. Jin, *Chem. Mater.*, 2021, **33**, 1994–2003.
58 L. Li, F. Lu, R. Xue, B. Ma, Q. Li, N. Wu, H. Liu, W. Yao, H. Guo and W. Yang, *ACS Appl. Mater. Interfaces*, 2019, **11**, 26355–26363.
59 P. Bhanja, K. Bhunia, S. K. Das, D. Pradhan, R. Kimura, Y. Hijikata, S. Irle and A. Bhaumik, *ChemSusChem*, 2017, **10**, 921–929.

60 S. Vargheese, M. Dinesh, K. V. Kavya, D. Pattappan, R. T. R. Kumar and Y. Haldorai, *Carbon Lett.*, 2021, **31**, 879–886.
61 Y. Liu, Z. Zhao, W. Xu and W. Gong, *Catal. Sci. Technol.*, 2024, **14**, 3211–3218.
62 M. G. Mohamed, S. U. Sharma, N. Y. Liu, T. H. Mansoure, M. M. Samy, S. V. Chaganti, Y. L. Chang, J. T. Lee and S. W. Kuo, *Int. J. Mol. Sci.*, 2022, **23**, 3174.
63 P. Kuhn, A. Thomas and M. Antonietti, *Macromolecules*, 2009, **42**, 319–326, DOI: **10.1021/ma802322j**.
64 A. O. Mousa, Z. I. Lin, C. H. Chuang, C. K. Chen, S. W. Kuo and M. G. Mohamed, *Int. J. Mol. Sci.*, 2023, **24**, 8966.
65 M. G. Mohamed, A. F. M. EL-Mahdy, M. M. M. Ahmed and S. W. Kuo, *ChemPlusChem*, 2019, **84**, 1767–1774.
66 M. G. Mohamed, A. F. M. El-Mahdy, Y. Takashi and S. W. Kuo, *New J. Chem.*, 2020, **44**, 8241–8253.
67 Z. Qinglan, W. Xianyou, W. Chun, L. Jing, W. Hao, G. Jiao, Z. Youwei and S. Hongbo, *J. Power Sources*, 2014, **254**, 10–17.
68 J. Hong, W. Xiaomin, G. Zhengrong and P. Joseph, *J. Power Sources*, 2013, **235**, 285–292.
69 X. Pan and D. C. Webster, *ChemSusChem*, 2012, **5**, 419–429.
70 P. Kuhn, M. Antonietti and A. Thomas, *Angew. Chem., Int. Ed.*, 2008, **47**, 3450–3453.
71 S. Mukherjee, M. Das, A. Manna, R. Krishna and S. Das, *Chem. Mater.*, 2019, **31**, 3929–3940.
72 L. Hao, J. Ning, B. Luo, B. Wang, Y. Zhang, Z. Tang, J. Yang, A. Thomas and L. Zhi, *J. Am. Chem. Soc.*, 2015, **137**, 219–225.
73 M. M. Samy, M. G. Mohamed and S. W. Kuo, *Eur. Polym. J.*, 2020, **138**, 109954.
74 M. G. Mohamed, M. Y. Tsai, W. C. Su, A. F. M. EL-Mahdy, C. F. Wang, C. H. Huang, L. Dai, T. Chen and S. W. Kuo, *Mater. Today Commun.*, 2020, **24**, 101111.
75 G. Wang, K. Leus, S. Zhao and P. Van Der Voort, *ACS Appl. Mater. Interfaces*, 2018, **10**, 1244–1249.
76 A. O. Mousa, C. H. Chuang, S. W. Kuo and M. G. Mohamed, *Int. J. Mol. Sci.*, 2023, **24**, 12371.
77 R. A. Maia, F. L. Oliveira, V. Ritleng, Q. Wang, B. Louis and P. M. Esteves, *Chem. – Eur. J.*, 2021, **27**, 8048–8055, DOI: **10.1002/chem.202100478**.
78 M. Ejaz, M. M. Samy, Y. Ye, S. W. Kuo and M. G. Mohamed, *Int. J. Mol. Sci.*, 2023, **24**, 2501.
79 M. M. Samy, M. G. Mohamed, S. U. Sharma, S. V. Chaganti, J. T. Lee and S. W. Kuo, *J. Taiwan Inst. Chem. Eng.*, 2024, **158**, 104750.
80 M. M. Samy, M. G. Mohamed, S. U. Sharma, S. V. Chaganti, T. H. Mansoure, J. T. Lee, T. Chen and S. W. Kuo, *Polymer*, 2023, **264**, 125541.
81 M. G. Mohamed, M. H. Elsayed, Y. Ye, M. M. Samy, A. E. Hassan, T. H. Mansoure, Z. Wen, H. H. Chou, K. H. Chen and S. W. Kuo, *Polymers*, 2023, **15**(15), 182.
82 M. M. Samy, M. G. Mohamed and S. W. Kuo, *Polymers*, 2023, **15**, 1095.
83 M. G. Mohamed, S. Y. Chang, M. Ejaz, M. M. Samy, A. O. Mousa and S. W. Kuo, *Molecules*, 2023, **28**, 3234.
84 M. Madhu, S. Santhoshkumar, C. W. Hsiao, W. L. Tseng, S. W. Kuo and M. G. Mohamed, *Macromol. Rapid Commun.*, 2024, 2400263.
85 T. H. Weng, M. G. Mohamed, S. U. Sharma, I. M. A. Mekhemer, H. H. Chou and S. W. Kuo, *ACS Appl. Energy Mater.*, 2023, **6**, 9012–9024.
86 P. N. Singh, M. G. Mohamed, S. V. Chaganti, S. U. Sharma, M. Ejaz, J. T. Lee and S. W. Kuo, *ACS Appl. Energy Mater.*, 2023, **6**, 8277–8287.